





Dynamics of Photospheric Magnetic Flux Distribution and Variations in Solar RVs: A Study Using HARPS-N Solar and SDO Observations

Anisha Sen^{1,2}  and S. P. Rajaguru^{1,3,4} ¹ Indian Institute of Astrophysics, II Block, Koramangala, Bengaluru 560 034, India; anisha.sen@iiap.res.in, rajaguru@iiap.res.in² Pondicherry University, R.V. Nagar, Kalapet, Puducherry 605014, India³ Department of Physics and W.W. Hansen Experimental Physics Lab, Stanford University, Stanford CA 94305, USA

Received 2023 March 25; revised 2023 August 14; accepted 2023 September 6; published 2023 October 18

Abstract

The distribution and evolution of photospheric magnetic fields in sunspots, plages, and network, and variations in their relative flux content, play key roles in radial velocity (RV) fluctuations observed in Sun-as-a-star spectra. Differentiating and disentangling such magnetic contributions to RVs help in building models to account for stellar activity signals in high-precision RV exoplanet searches. In this work, as earlier authors, we employ high-resolution images of the solar magnetic field and continuum intensities from SDO/HMI to understand the activity contributions to RVs from HARPS-N solar observations. Using well-observed physical relationships between strengths and fluxes of photospheric magnetic fields, we show that the strong fields (spots, plages, and network) and the weak inter-network fields leave distinguishing features in their contributions to the RV variability. We also find that the fill factors and average unsigned magnetic fluxes of different features correlate differently with the RVs and hence warrant care in employing either of them as a proxy for RV variations. In addition, we examine disk-averaged UV intensities at 1600 and 1700 Å wavelength bands imaged by SDO/AIA and their performances as proxies for variations in different magnetic features. We find that the UV intensities provide a better measure of contributions of plage fields to RVs than the Ca II H-K emission indices, especially during high activity levels when the latter tend to saturate.

Unified Astronomy Thesaurus concepts: [Solar photosphere \(1518\)](#); [Radial velocity \(1332\)](#); [Solar activity \(1475\)](#); [Solar active region magnetic fields \(1975\)](#)

1. Introduction

The radial velocity (RV) technique measures the Doppler shifts in the spectrum of a host star to derive its wobble motion caused by the orbital motion(s) of planet(s) around it. Since its use in the first definitive exoplanet detection (Mayor & Queloz 1995), it has remained a key tool in the discovery and characterization of exoplanetary systems. Major efforts are currently underway toward achieving extreme precision RV (EPRV) of centimeters per second needed to detect Earth-size planets around Sun-like stars (Newman et al. 2023) (see also NASA EPRV Working group final report, Crass et al. 2021). However, it is also well recognized that convective flows and magnetic activity in the photospheres of host stars cause RV fluctuations, known as astrophysical noise or jitter, much larger than the wobble signals caused by the orbital motion of a planet (Boisse et al. 2011; Luhn et al. 2023). The RV contributions from stellar surface magnetic fields are intimately related to one of the fundamental effects in magnetohydrodynamics (MHD), viz. magnetic forces modifying the fluid motion. In stars with outer convection zones, like the Sun, fluid motion at the photosphere is in the form of convective granules, which have the upward-moving spectrally blueshifted, hotter less dense plasma occupying a much larger area than the downward-moving redshifted, denser, and cooler plasma at their

boundaries (Dravins et al. 1981). As the flux or area coverage (fill factor) of strong enough magnetic fields increases, the effects of magnetic suppression of plasma motions dominantly appear as a reduction in the convective blueshift of photospheric spectral lines due to the fact that most of the stellar light comes from the bright blueshifted plasma (Cegla et al. 2018; Cegla 2019). In addition, the magnetic fields themselves, depending on their sizes and strengths, introduce their own thermal changes and hence in their brightnesses: dark spots and bright faculae, which can cluster to form bright plages, can differ in their relative contributions to the above suppression of convective blueshifts and hence to RVs (Dumusque et al. 2014; Haywood et al. 2016; Meunier et al. 2017). Further complications can arise from additional characteristic flows, such as large amplitude Evershed flows, the not-so-dark penumbrae of spots harbor. There is also the additional component of more uniformly distributed supergranular and intergranular magnetic network, commonly known in the solar physics literature as network and inter-network (IN), which can still interfere with convective motions in a manner that may depend on their size (flux) and strength distribution. These network magnetic elements, more uniformly distributed over the stellar disk, do not cause significant photometric modulation, except over the timescales of the solar cycle. Clearly, there is a complicated set of MHD processes at play resulting in delicate imbalances in the photometric and spectroscopic signatures of different magnetic structures and hence in their contributions to RVs (Apai et al. 2018).

For distant stars, we cannot directly observe the surface phenomena and hence cannot observationally remove the above stellar surface contributions to RVs, so the RV method is severely limited by the effects of stellar magnetic activity.

⁴ A major part of this work was completed when S.P.R. was on sabbatical at Stanford University.



Clearly, retrieval of a planetary wobble signal in RVs requires a good understanding and modeling of all the contributions from the stellar surface magnetic fields of differing strengths and fluxes. The Sun, the only star on which we can directly observe in a resolved manner the different magnetic structures, is an excellent test case that allows us to investigate the stellar RV fluctuations. It is exactly for this purpose that the solar feed to the High Accuracy Radial-velocity Planet Searcher for the Northern hemisphere (HARPS-N) instrument was designed for independent spectroscopic measurements of solar RVs (Dumusque et al. 2015). Solar observations at HARPS-N began in 2015 July and the first 3 yr of solar RVs derived from several hours of observations each day have been released and are publicly accessible via the Data and Analysis Center for Exoplanets⁵ hosted at the University of Geneva. Using the first release of RVs derived using the HARPS-N Data Reduction System (DRS) along with contemporaneous disk-resolved continuum intensity and magnetic field data from Helioseismic and Magnetic Imager (HMI)/Solar Dynamics Observatory (SDO) and Total Solar Irradiance (TSI) data from SORCE Total Irradiance Monitor (TIM), Milbourne et al. (2019) have shown that the HARPS-N solar RV fluctuations arise mainly due to the large and bright magnetic regions occupying areas larger than 60 Mm² and that the smaller structures do not significantly contribute. In addition, they also showed that the chromospheric Ca II H-K flux index $\log(R'_{\text{HK}})$ and the optical light curves would provide effective proxies for RV variations in the plage-dominated stars but not in the case of the low-activity stars, where the plage and network filling factors are comparable. Prior to that, using solar RVs derived from HARPS observations of sunlight scattered off the bright asteroid 4/Vesta, Haywood et al. (2016) found that the RV variations induced by solar activity were mainly due to the suppression of convective blueshift from magnetically active regions. They also found that the disk-averaged line-of-sight (LOS) magnetic flux was a better proxy for the activity-driven RV variations than the FWHM and BIS of the cross-correlation profile and the Ca II H and K activity index. In their latest study, Haywood et al. (2022) concluded that the unsigned magnetic flux was an excellent proxy for RV variations.

The difficulties of differentiating and disentangling contributions of magnetic spots, plages/faculae, and more uniformly distributed network structures to the RVs were further highlighted by Milbourne et al. (2021), who concluded that more detailed information on the feature-specific filling factors is needed to fully characterize the host stars through the spectroscopic and brightness indices such as S-index and TSI. As alluded to earlier, the highly nonuniform distribution of magnetic fields, in strengths and sizes, accompanied by their differing thermal (brightness) signatures is behind the above difficulties. In the present analysis, we factor in some of the well-studied physics behind the magnetic structuring of the solar atmosphere while extracting feature-specific filling factors from the high-resolution magnetic and intensity images of the Sun from the HMI and Atmospheric Imaging Assembly (AIA) on board SDO. We use the latest release of HARPS-N solar data calibrated using ESPRESSO DRS 2.3.5 (Section 2) and examine more closely their correlated variations with different feature-specific fill factors and average unsigned magnetic fluxes with a focus on assessing the contributions of

intrinsically weak magnetic features, known in the solar physics literature as IN fields, which are known to contribute to brightness variations in certain wavelength bands (Bellot Rubio & Orozco Suárez 2019). In general, we focus on the dynamical relationships between the flux distribution of different features, especially on the timescales of decay of strong fields into weak fields, and their possible signatures in RV variations. We attempt to factor in established physics behind flux-strength relationships of surface magnetic structures to gain a better understanding of the range and magnitude of RV fluctuations that can be expected in Sun-like stars with varying levels of interactions between convection and magnetic fields.

This paper is organized as follows: Section 2 gives descriptions of the data used followed by Section 3 describing the methods adopted for the analysis, especially a detailed description of our new methods to identify the weak IN magnetic fields from HMI observations in Section 3.1. We present our results in Section 4 with subsections devoted to our new findings on (i) variations of, and connections between, feature-specific fill factors and average unsigned magnetic fluxes, (ii) correlations between the SDO/HMI-derived magnetic quantities and RVs and Ca II H-K flux indices $\log(R'_{\text{HK}})$ derived from HARPS-N observations, (iii) a detailed analysis of new disk-averaged 1600 and 1700 Å UV intensities from SDO/AIA observations as magnetic proxies for RV variations, and (iv) on Lomb–Scargle periodogram analysis of timescales of variations from magnetic features that are correlated with that in RVs, $\log(R'_{\text{HK}})$ s and also the SORCE TSI variations. Detailed discussions and our conclusions are presented in Section 5.

2. Data

2.1. HARPS-N Solar Observations

HARPS-N is a high-precision RV spectrograph installed at the Italian Telescopio Nazionale Galileo (TNG), a 3.58 m telescope located at the Roque de Los Muchachos Observatory on the island of La Palma, Canary Islands, Spain. Since 2015 July 18, with its solar feed, HARPS-N has observed the Sun every day with a 5 minute cadence (Dumusque et al. 2015). We have used these Sun-as-a-star spectroscopic data from the HARPS-N (Phillips et al. 2016; Collier Cameron et al. 2019), as calibrated and released using the latest version of the pipeline ESPRESSO DRS 2.3.5 (Dumusque et al. 2021). This release covers roughly a 3 yr period between 2015 July 18 and 2018 December 31. We use the pipeline-extracted RVs and the chromospheric flux index $\log(R'_{\text{HK}})$ (Noyes et al. 1984). The above data are publicly accessible at the Data and Analysis Center for Exoplanets⁶ hosted at the University of Geneva.

2.2. SDO Observations

SDO is a NASA spacecraft that has been observing the Sun since 2010 March. HMI (Scherrer et al. 2012) on board SDO observes the photosphere while the other two instruments, AIA (Lemen et al. 2011) and Extreme Ultraviolet Variability Experiment observe the chromospheric and coronal layers in various UV and EUV wavelength bands. Data from this mission is publicly available.⁷ For our analysis, we use HMI

⁵ <https://dace.unige.ch>

⁶ <https://dace.unige.ch>

⁷ <http://jsoc.stanford.edu/>

and AIA observations of the photosphere and chromosphere, respectively, for the same dates as HARPS-N Sun-as-a-star spectroscopic observations. HMI makes full-disk photospheric observations of continuum intensity, LOS (Doppler) velocity, and magnetic fields at 45 s cadence, and also all the Stokes parameters to derive the vector magnetic field at 135 s cadence (although the standard data product is at 720 s cadence). The above observables are derived from imaging over six wavelength positions across the Fe I 6173 Å line at a spatial resolution of 1'' (pixel size of 0''.5) using a 4×4 K CCD for each of the LOS and vector quantities (Wachter et al. 2011; Liu et al. 2012; Scherrer et al. 2012; Schou et al. 2012). We have used HMI LOS magnetograms with a cadence of 45 s and limb-darkening-removed continuum intensities extracted at 720 s cadence. We use AIA full-disk UV intensities at the wavelengths 1700 and 1600 Å, which image the upper photospheric and lower chromospheric layers with mean formation heights of 360 and 430 km above the photosphere (Fossum & Carlsson 2005), respectively. AIA observes these wavelengths at a cadence of 24 s (Lemen et al. 2011).

The HMI LOS magnetograms and continuum intensities are used for identifying and separating different features on the solar surface and the UV intensities from AIA to estimate disk-averaged chromospheric emissions due to magnetic fields. We extract 24 observations per day (one image per hour), spread over the duration between 2015 January 1 to 2018 December 31, from both the instruments (HMI and AIA), and average the derived quantities (as in Section 3) for each day.

2.3. *SORCE/TIM TSI Observations*

Simultaneous high-accuracy Sun-as-a-star photometric observations are well known as key measures of solar activity variations from days and months to solar cycle timescales. Such information is also crucial to assess the relative contributions of different magnetic features, bright and dark, to the RV variations. For this purpose, and especially to ascertain further some of our newly identified contributions from weak IN fields, we employ TSI measurements by TIM on board the SORCE satellite (Kopp & Lawrence 2005; Kopp et al. 2005). TSI data from SORCE/TIM are publicly available,⁸ and we employ a contemporaneous 24 hr cadence time series of this data in our analysis.

3. Method of Analysis

A primary aim of this work is to factor in some well-studied physics behind the flux and strength distributions of solar surface magnetic fields, especially on small spatial scales and flux contents, while identifying and estimating feature-specific fill factors and their average unsigned magnetic fluxes thereby improving our understanding of their contributions to RVs. To this end, and also to compare with previous results, we follow the same basic steps in the preparation and processing of SDO/HMI full-disk images as originally done by Haywood et al. (2016) and adopted in various follow-up studies (e.g., Milbourne et al. 2019, 2021; Haywood et al. 2022). We briefly describe the basic processing steps below, followed by a description of new features in our analysis in Section 3.1.

We convert SDO images from pixel coordinates to heliographic coordinates (a coordinate system centered on the

Sun; Thompson 2006) and employ a built-in routine *aiaprep* available in the SunPy packages (Barnes et al. 2020) to align the HMI and AIA images to a same spatial scale. We crop the HMI as well as the AIA images at a center-to-limb distance of $0.96 R_{\odot}$ to avoid noisy pixels near the limb. For the AIA images, we employ a median filtering method (Lefebvre et al. 2005; Bertello et al. 2010; Chatterjee et al. 2016; Bose & Nagaraju 2018) to remove limb darkening. Following Haywood et al. (2016), assuming that much of the magnetic flux on the solar surface is vertically oriented, we convert the HMI LOS magnetic field strength B_{obs} to radial magnetic field strength B_r by removing the foreshortening effect, $B_{r,ij} = B_{\text{obs},ij}/\mu_{ij}$, where $\mu_{ij} = \cos \theta_{ij}$ and θ_{ij} is the angle between the outward normal on the solar surface and the direction of the LOS from the SDO spacecraft. The upper left panel of Figure 1 shows an unsigned radial magnetogram, after correcting the foreshortening effects, the upper right panel shows limb-darkening-corrected HMI continuum intensity, and the middle panels show limb-darkening-corrected AIA 1600 Å (left panel) and 1700 Å (right panel) intensities. These images are from 2015 January 1. The noise level in HMI magnetograms is the lowest for pixels near the center of the CCD (around 5G) and increases toward the edges, reaching 8G at the solar limb (Yeo et al. 2013). Denoting the magnetic noise level in each pixel as $\sigma_{B_{\text{obs},ij}}$, we set $B_{\text{obs},ij}$ and $B_{r,ij}$ to 0 for all pixels with a LOS magnetic field measurement $B_{\text{obs}} < \sigma_{B_{\text{obs},ij}} = 8G$ (Haywood et al. 2016). Yeo et al. (2013) investigated the intensity contrast between the active and quiet photosphere using SDO/HMI full-disk images and found a cutoff at $|B_{r,ij}| > 3\sigma_{B_{\text{obs},ij}}/\mu_{ij}$. The separation of magnetic pixels from nonmagnetic or quiet ones follows this 3σ criterion, $|B_{r,\text{thresh1},ij}| = 24G/\mu_{ij}$, and the further division of magnetic pixels into bright faculae and dark sunspots follows the same intensity thresholding criteria employed by Yeo et al. (2013) and Haywood et al. (2016): $I_{\text{thresh}} = 0.89I_{\text{quiet}}$, where $I_{\text{quiet}} = \frac{\sum_{ij} I_{\text{flat},ij} W_{ij}}{\sum_{ij} W_{ij}}$ with weighting factor $W_{ij} = 1$ if $|B_{r,ij}| < |B_{r,\text{thresh1},ij}|$ and $W_{ij} = 0$ otherwise. In the lower-left panel of Figure 1, we show a thresholded image separating the sunspot (in black) from all the other fields (in purple). In the next step, we apply area thresholding to split the non-spot fields into plages and network: contiguous field patches exceeding an area threshold of 20 μ -hemispheres or 60 Mm^2 , the same as the one employed by Milbourne et al. (2019), are identified as plages (green patches in the lower right panel of Figure 1).

3.1. *Identification of Weak IN Magnetic Fields in HMI Observations*

The above processing steps separate flux outside of sunspots into bright ($I > I_{\text{thresh}}$) plages (area $> 60 \text{Mm}^2$) and all of the rest as network (Milbourne et al. 2019, 2021; Haywood et al. 2022). However, it is well known that the quiet-Sun magnetic field on the solar surface has two fundamentally different distributions, in terms of their intrinsic strength and flux, due to their interaction with supergranular convection (Lin 1995; Solanki et al. 1996, see Bellot Rubio & Orozco Suárez 2019 for a detailed review): the quiet-Sun fields in the cell interior of supergranules, referred to as IN, are weak with typically less than or equal to the photospheric equipartition (kinetic) strengths of about 400–500 G with flux content in the range of 10^{16} —a few times 10^{17} Mx, while the network (NE, hereafter) fields confined to the boundaries of supergranules are made up

⁸ <https://lasp.colorado.edu/home/sorce/data/tsi-data/>

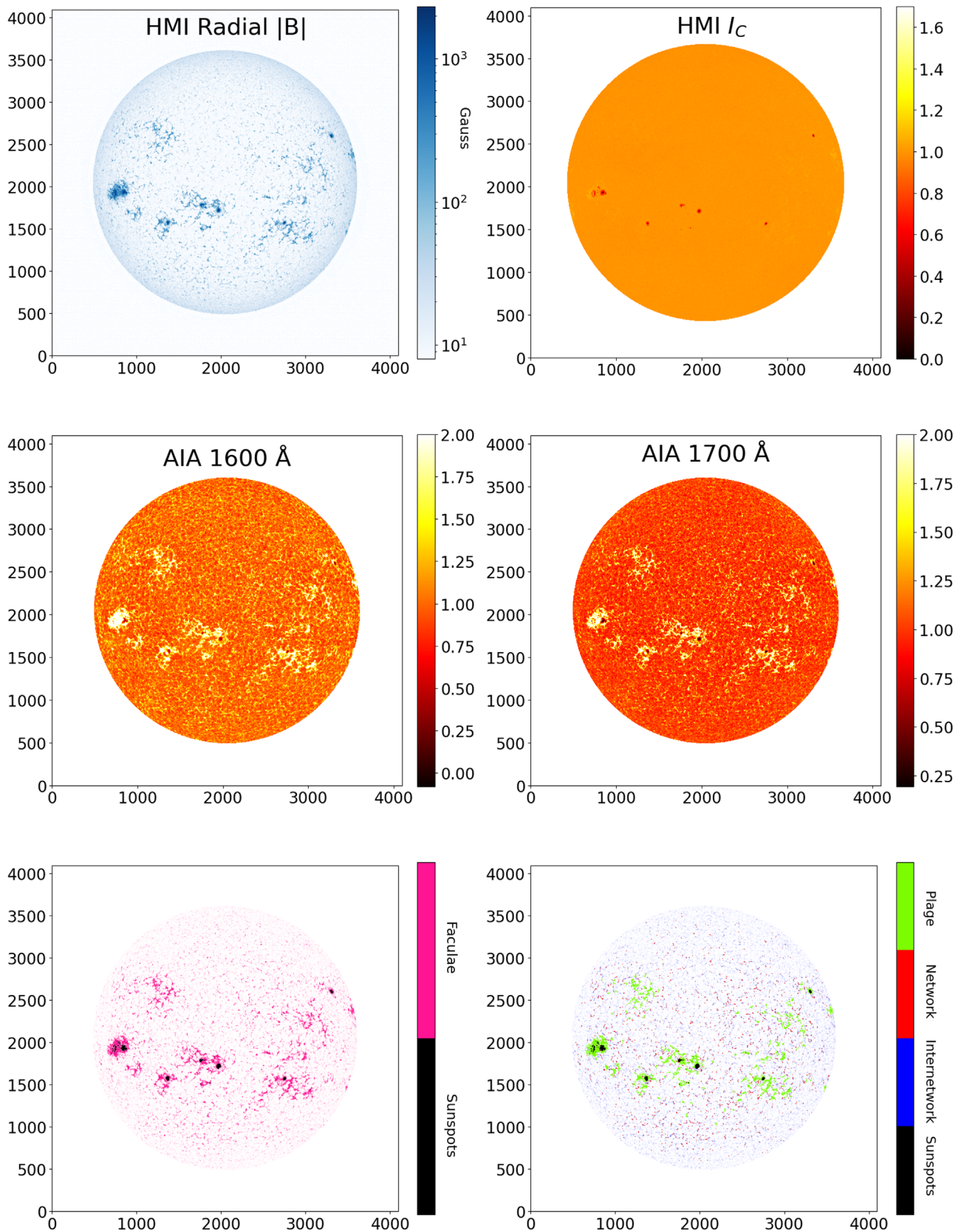


Figure 1. Sample images of SDO observables, from the 2015 January 1: radial magnetic fields from SDO/HMI LOS magnetogram (top left panel) and limb-darkening-corrected continuum intensity (top right panel), SDO/AIA intensities at 1600 Å (middle left panel) and at 1700 Å (middle right panel). The color bar for HMI continuum intensity and AIA images saturate at a value well below the maximum value. The lower panels show thresholded images for the same date: the left panel shows sunspots and all the rest of the magnetic fields based on the thresholding criteria of Haywood et al. (2016), while the right panel shows the non-sunspot fields separated into plage, network, and weak IN based on our new thresholding criteria explained in Section 3.1.

of flux elements that have undergone *convective collapse* (Parker 1978; Spruit 1979) attaining super-equipartition kilo-Gauss strengths with flux content typically larger than about a few time 10^{17} Mx. A detailed observational study (Solanki et al. 1996) of field strength versus flux relationship of small-scale fields gives a rough flux limit of $\sim 3 \times 10^{17}$ Mx that separates the collapsed kilogauss fields (NE) from partially collapsed intermediate strength or weaker IN fields. Such an organization of small-scale magnetic flux also has a sound theoretical basis, which derives from the effects of radiative smoothing on the convective collapse mechanism (Venkatakishnan 1986; Rajaguru & Hasan 2000). Recent very high-resolution and high polarimetric sensitivity observations (Gošić et al. 2014; Prabhu et al. 2020; Campbell et al. 2021) confirm the above basic characteristics of NE and IN magnetic fields in the solar photosphere, and also give a resolved picture of a typical weak IN field: it is a low-lying small loop with its highly inclined (linear polarization causing) segment, over a granule, flanked by vertical (circular polarization causing) field within intergranular lane. A typical NE field element is a vertical structure rooted in the supergranular boundary and extending high into the chromospheric layers.

At the HMI resolution of $1''$, IN fields with a flux limit of 3×10^{17} Mx will present themselves with strengths up to 56 G ($= 3 \times 10^{17}$ Mx / $(7.3 \times 10^7 \text{ cm})^2$). Although the early studies that established the presence and properties of IN fields were done at $1''$ – $2''$ resolution (Lites et al. 1996; Lites 2002), current understanding gained from high-resolution observations (Bellot Rubio & Orozco Suárez 2019) shows that observations start to resolve the IN fields at $1''$ resolution, that there exists much more IN flux at still smaller scales, and that the average filling factors increase as resolution increases. This aspect of IN fields is now well established, especially after the Hinode space mission enabled detailed measurements of quiet-Sun magnetic flux (Lites et al. 2008), which was also shown to require a local dynamo distinct from the one generating the active region flux. Our results here (presented in the following sections) show that, despite its lower resolution of $1''$, HMI does capture a significant amount of IN flux. And as we show in later sections, we are able to distinguish the differing signatures of IN and NE fields in the HARPS-N RV variations.

We note that the basic step in the analysis of Haywood et al. (2016) converting the HMI LOS magnetic field strength B_{obs} to radial magnetic field strength B_r , assumes that most of the flux in the HMI magnetograms is vertically oriented. This assumption is still reasonable as high-resolution observations discussed above do indeed show circular polarization signals arising from the vertically oriented legs of IN fields, although it is expected that the $\mu_{ij} = \cos \theta_{ij}$ correction may overcorrect the contributions from the horizontal parts of IN field loops, which align to LOS as center-to-limb distance increases. However, such systematics is taken care of as we do include the μ_{ij} factor to the threshold of 56 G estimated from the above-discussed flux limit of $\sim 3 \times 10^{17}$ Mx that separates the weak and strong (super-equipartition) fields. Thus, in our final step, we split the non-spot ($I > I_{\text{thresh}}$ and $B > |B_{r,\text{thresh}1,ij}|$) and non-plage magnetic (area $< 60 \text{ Mm}^2$) pixels into NE and IN fields depending on their magnetic flux density: those greater than the threshold value, $|B_{r,\text{thresh}2,ij}| = 56 \text{ G} / \mu_{ij}$, are grouped as stronger NE fields and the rest as weak IN fields. In the lower right panel of Figure 1, we show the result of the above

segmentation criteria that results in separated spot, plage, NE, and weak IN regions.

4. Results

4.1. Feature-specific Fill Factors and Average Unsigned Magnetic Fluxes

A basic feature in our analysis, distinct from previous ones, of HMI magnetic field observations is the identification and separation of the IN fields, as explained in the previous section. Figure 2 shows the fill factors of IN, NE, plage, and spot fields for the full 4 yr period (1437 days) between 2015 January and 2018 December. Note that the HARPS-N observations (shown in later figures) cover a subset of days, totaling about 609 days, within this period (due to missing days and a longer gap toward the end). We have also calculated feature-specific average unsigned magnetic fluxes, $\langle |B_m| \rangle = \frac{\sum_{ij} |B_{m,ij}|}{N_m}$, where the subscript m stands for spot, plage, NE, or IN, $B_{m,ij}$ is the pixel field strength and N_m is the total number of pixels occupied by feature m . The disk-averaged unsigned magnetic flux of the different features is then $f_m \langle |B_m| \rangle$, which we simply write as $(fB)_m$ and plot them in Figure 3. The total disk-averaged unsigned magnetic flux is then $\langle |B| \rangle = \sum_m f_m \langle |B_m| \rangle$, which is simply the sum of the different panels of Figure 3. The starting date (2015 January) falls during moderately high activity—about a year after the maximum of Solar Cycle 24, and the ending date in 2018 December is around the cycle minimum, and hence all the quantities, including the RVs and $\log(R'_{\text{HK}})$ from HARPS-N, show a clear decline over the analysis period. Variation at solar rotation period is dominant in the feature-specific fill factors f_m and average unsigned magnetic fluxes $(fB)_m$ shown in Figures 2 and 3—the overplotted smooth curves in black in the different panels correspond to longer timescale variation obtained after a Fourier filter (low-pass filter) to remove periods shorter than 60 days.

We note several interesting and dominant patterns along with subtle but still easily discernible differences and similarities between the features: (i) the relative change in IN fields, over the longer cyclic timescale, is an order of magnitude less compared to those of other features, (ii) the IN fields show shorter timescale noise-like fluctuations, (iii) within the intermediate timescales of longer than rotation and up to a year, the IN and NE fields show a correlated variation on the longer period side while the plage and spot fields correlate tightly on timescales of a few months, (iv) spots show larger fluctuations on the rotation as well as slightly shorter and longer timescales, and (v) there are intermittent instances highly correlated variation, with a few days to a week of time lag, between spots and the IN fields (see the insets in Figures 2 and 3)—the two large peaks in f_{IN} and $(fB)_{\text{IN}}$ are associated with a similar increase in f_{spot} and $(fB)_{\text{spot}}$ about a week earlier, while there is no such correlation between spots and NE at these two instances. The above-noted features carry important information on the dynamical connections between the evolution of these different magnetic flux concentrations and their interactions with convective and other large-scale flows on the Sun. In the context of RV variations, which we address in the sections that follow, we particularly note the short timescale fluctuations of IN fields, which $+-^*$ at the same time change relatively little over the longer solar cycle timescale compared to other features. This latter aspect of IN fields is also well appreciated in the solar literature

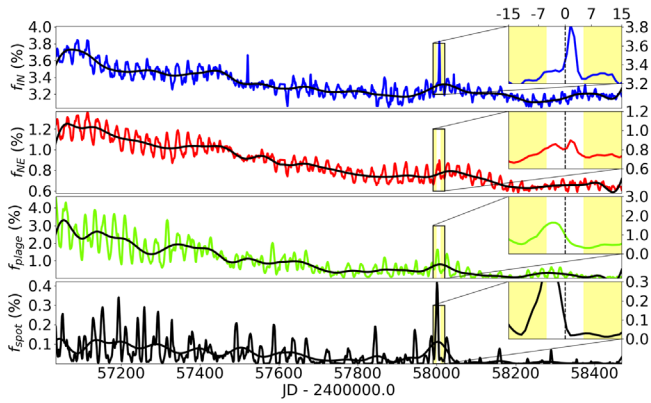


Figure 2. Feature-specific fill factors, f_m , derived from full-disk SDO/HMI observations (top to bottom): weak IN (IN), strong network (NE), plage, and sunspot fields. The overplotted black curve in each panel is a smoothed one retaining only variations longer than 60 days obtained with a low-pass Fourier filter. The insets in each panel show a zoomed-in view of a selected 30-day window around a large increase in spot flux and its connections to other features.

(Bellot Rubio & Orozco Suárez 2019). We discuss further these features in Section 4.4, where we analyze the timescales involved through periodograms.

To understand further and check the new features of our analysis, we compare our estimates of f_m in Figure 2 with those of Milbourne et al. (2021) and Haywood et al. (2022), especially for the network flux, which in our analysis have been separated into weak IN and strong NE. We find that the sum $f_{IN} + f_{NE}$ of IN and NE fill factors (sum of the top two panels of Figure 2) is more than twice the estimate for f_{ntwk} in Figure 2 of Milbourne et al. (2021; or Figure 4 of Haywood et al. 2022) while the plage (f_{plage}) and spot (f_{spot}) fill factors match closely. Since this is a rather large discrepancy, we set out to examine all the differences in the way the data were processed and analyzed. We find that our results and that of Haywood et al. (2016) match exactly for fill factors of spot and all non-spot fields, which are termed faculae by Haywood et al. (2016), while all the later studies published by Milbourne et al. (2019), Milbourne et al. (2021), and Haywood et al. (2022) show the above discrepancy that we have noted for the network fields (IN and NE). A careful examination reveals that all these later studies have employed 720 s cadence data, while ours here and that of Haywood et al. (2016) use the original 45 s cadence data from HMI. We clarify that the 720 s HMI data are actually averages of 45 s cadence basic observations over 720 s (Hoeksema et al. 2014). Hence, noting that IN fields are typically moved around by granules with typical lifetimes of 5–10 minutes, it is expected that the 12 minutes (720 s) averaging of HMI observations will smooth out the IN fields due to granular timescale displacements as well as due to cancellations of opposite polarity signals passing through a given location over this time interval. Hence, the use of 720 s exposure data from HMI will yield significantly reduced values for the fill factors of IN fields (f_{IN}), and this certainly plays a role in the much-reduced values for f_{ntwk} of Milbourne et al. (2021). To test this explicitly, we have repeated our analysis using the 720 s exposure data from HMI, and the results and comparisons are presented in Appendix in a table and in a figure. In summary, we now find that the total network flux (IN + NE flux), $f_{IN} + f_{NE}$, which we find in our main analysis (in Figure 2), is much larger than those reported by Milbourne et al. (2021) and Haywood et al. (2022) mainly because the

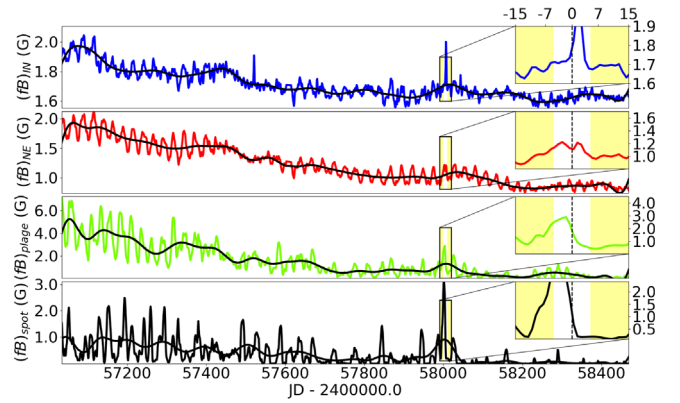


Figure 3. Feature-specific disk-averaged unsigned field magnetic fluxes, $(fB)_m = f_m \langle |B_m| \rangle$, in the same order (top to bottom), with the overplotted black curves obtained in the same way, as in Figure 2. The insets are the same as explained in the caption of Figure 2.

latter authors used HMI magnetograms averaged over 12 minutes, which misses much of the weak IN fields evolving over granular convection timescales. Further, as we show in Appendix, fill factors (f_{NE}) of stronger (or collapsed) NE fields do not show any difference between the use of 45 or 720 s cadence HMI data because the NE fields typically have a much longer lifetime (20 minutes or longer) than the IN fields (Bellot Rubio & Orozco Suárez 2019). This reaffirms that our method to separate the weak (IN) and strong (NE) network fields based on a flux criterion has indeed worked successfully. We conclude that our identification criteria respecting the physics behind the dynamics of small-scale magnetic fields along with our use of original 45 s cadence and 1'' resolution HMI data, compared to the 12 minute averaged and a likely lower effective resolution (due to 2×2 binning) employed by Milbourne et al. (2019), Milbourne et al. (2021), and Haywood et al. (2022) have facilitated capturing especially the weak IN fields, which are missed in these earlier measurements. This weak component of network fields, as we show below, carries a large fraction of total solar magnetic flux but changes slowly over the solar cycle timescale, and hence, is important to determine the base level of RV fluctuations due to magnetism. Note that differences in temporal and spatial resolutions do not affect measurements of plages and spots and hence we match earlier measurements for these larger features.

To elucidate further the connections between different magnetic features, we plot in Figure 4 the relative contributions of individual f_m and $(fB)_m$ to the total for the whole Sun. First, the results here indeed show that there is a significant fraction of solar magnetic flux in the IN as evidenced in the bottom panel of Figure 4: at cycle maximum about 20%–25% of solar magnetic flux is in the weak form, which increases to more than 50% near cycle minimum. In terms of numbers for the fluxes, we find that, within the time period of observations covered, the IN and NE fields have similar amounts of flux, $0.8\text{--}1.2 \times 10^{23}$ and $0.5\text{--}1.3 \times 10^{23}$ Mx, respectively (see the right panel of Figure 5). High-resolution observations by Zhou et al. (2013), Gošić et al. (2014) estimate that IN fields carry a total flux of the order of $\sim 1.1 \times 10^{23}$ Mx and NE fields at a much higher value of $\sim 6.8 \times 10^{23}$. This shows that HMI, at 1'' resolution, misses a significant amount of network fields (IN and NE fields), especially much of the very small-scale collapsed kilogauss strength NE fields. It is also possible that the flux limit of 3×10^{17} Mx and hence the HMI flux density of

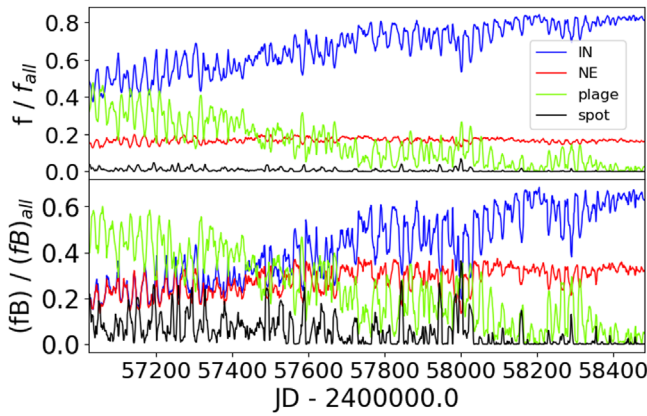


Figure 4. Time evolution of relative areas, f/f_{all} , and average unsigned magnetic fluxes, $(fB)/(fB)_{\text{all}}$, over the 4 yr period of 2015 January–2018 December.

56 G that we used to separate IN from NE fields is not accurate, implying there still exist kilogauss fields (i.e., NE) at lower flux contents. In this situation, our identified IN and NE fields may have intermixed contributions. In any case, HMI measurements yielding a lower flux for IN and NE fields together is expected and it is certainly due to the lower resolution and thereby missing some scale-scale weak as well as strong flux. For active regions (spots + plages), our estimated flux is $\sim 6.5 \times 10^{23}$ Mx at the maximum activity level within the time period covered in Figure 5. This compares well with similar estimates ($\sim 6\text{--}8 \times 10^{23}$) for cycle maximum (Schrijver & Harvey 1994; Gošić et al. 2014), noting that the maximum activity level we have in our data is about 1 yr past the Cycle 24 maximum.

4.1.1. Correlations between Magnetic Fluxes, Fill Factors, and Strengths

The dependence of the intrinsic field strength of a solar magnetic structure on its flux content is a key relationship that derives from the physics of magnetic field intensification in the near-surface layers (Parker 1978; Venkatakrishnan 1986; Solanki et al. 1996; Rajaguru & Hasan 2000) and we used that to separate the weak IN fields as discussed in Section 3.1. Despite carrying a large amount of flux (see Figure 3), since they are in a shredded weak form at sub-granular scales, the IN fields interfere with convection in a different manner than the collapsed strong fields comprising plages and spots: for these latter structures increasing flux primarily increases their areas (fill factor) replacing the convective granules and thus directly contributing to the reduction of convective blueshift (and thus to RV variations). The transition between weak fields to strong fields is not sharp, but through a characteristic relationship between flux and strengths (Venkatakrishnan 1986; Solanki et al. 1996; Rajaguru & Hasan 2000), which we indeed see exhibited by the network fields: Figure 5 shows the relationship between the unsigned average field strengths ($|B_m|$) and fill factors (f_m) (left panel) and total fluxes ($(fB)_m \times \text{area}_{\odot}$, right panel) for the different features along with that for the whole of magnetic fields on the Sun. First, we note that our flux-per-feature criterion (3×10^{17} Mx or 56 G pixel strength at HMI resolution) has indeed very well separated the weak IN field from the strong NE fields, which have the same strengths as plage fields and differ only in their sizes (flux contents). Second, as expected, the average unsigned field strengths of

spots and plages show no trends against fill factors (areas) or their flux contributions, whereas those of network fields (IN and NE) show a strong correlation. The above flux-strength relation for the whole of the magnetic field is also plotted in Figure 5 (data points in pink color), and it is clear that the exponentially increasing flux contributions over the higher end of $|B| = 100\text{--}150$ G are mainly from collapsed strong fields of NE, plages, and spots. This relationship is essentially the same one as that studied by Solanki et al. (1996) in their high-resolution observations of weak IN and the stronger partially or fully collapsed NE field elements, and we have here verified it in HMI data. These correlations between fill factors f_m and average unsigned magnetic fluxes $(fB)_m$ have to be taken into account while assessing any correlations between f_m or $(fB)_m$ and the RV variations, ΔRV , presented in the next section.

4.2. Correlations between HARPS-N RVs and SDO/HMI Magnetic Field Observations

From the time series of RVs from HARPS-N, which has covered about a 609 days period between 2015 July 29 and 2018 July 16, in Figure 6 we compare the variations of mean-subtracted ΔRV ($RV - \langle RV \rangle$) and $\log(R'_{\text{HK}})$ with those of feature-specific average unsigned magnetic fluxes $(fB)_m$ estimated from HMI/SDO observations. For this comparison, we use the sum of all $(fB)_m$ with and without the IN field ($(fB)_{\text{IN}}$) and label them as (strong + weak) and (strong) fields, respectively; for a meaningful comparison here, since it is of different physical quantities and we need only their relative variations, we normalize a $(fB)_m$ by its maximum value. While a very good correlation at rotation timescales between these quantities is obvious, we note that, more importantly, on longer timescales, the inclusion of IN magnetic fields (black curve) matches the variations in ΔRV and $\log(R'_{\text{HK}})$ much more closely than without them (green curve). Such a contribution from IN fields is expected because the flux contained in them is significant (see Figure 3) and moreover they dominate the total flux during the solar minimum period as evident in the relative variations of $(fB)_m$ shown in Figure 4. Thus, the IN fields change relatively little over the solar cycle amounting to a nearly constant background flux on the Sun and cause a long-term background signal in ΔRV . However, we note that the true level of this background IN flux and hence the minimum or base level of variations in the mean-subtracted RVs do require covering fully a solar cycle minimum period. Otherwise, any accounting of relative variations in ΔRV that are biased by larger variations of active region fluxes would suffer from a long-term offset as can be seen in Figure 6. It is also clear (from the bottom panel of Figure 6) that the correlation between $\log(R'_{\text{HK}})$ and the full magnetic flux (strong + weak fields) is much cleaner and tighter than that between ΔRV and the magnetic flux. This is largely due to the shorter timescale noise-like fluctuations in ΔRV .

Next, we examine scatter plots of ΔRV ($RV - \langle RV \rangle$) and the feature-specific f_m and $(fB)_m$ and their correlation coefficients: the top row of Figure 7 shows ΔRV against f_m while the bottom row is that between ΔRV and the unsigned average magnetic flux $(fB)_m$. For each plot, we computed the Spearman correlation coefficients to measure the degree of correlation between two variables. Plage fields, in conformity with previous results (Milbourne et al. 2019), show the largest correlation (~ 0.75) with the variations in ΔRV . Importantly, variations in IN fields show a significant correlation (~ 0.6)

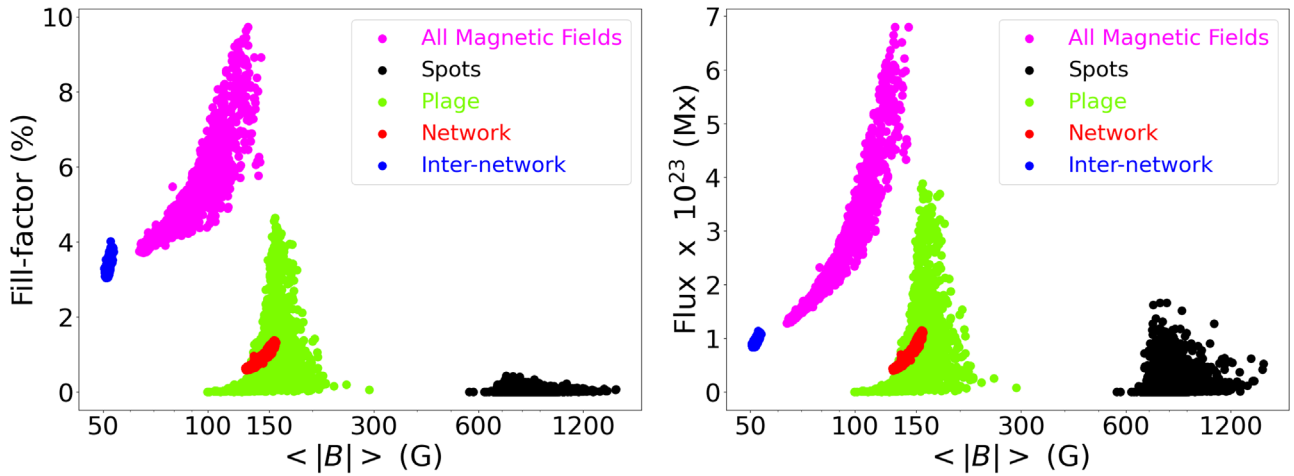


Figure 5. Relation between area fill factors (f_m , left panel) or total magnetic fluxes (right panel) of different magnetic features and their disk-averaged unsigned field strengths ($\langle |B| \rangle$).

with that in ΔRV . We note that the ΔRV are, in general, better correlated with fill factors f_m than with the average unsigned fluxes $\langle fB \rangle_m$. Further, the reduction in the correlation between ΔRV and $\langle fB \rangle_m$ compared to that between ΔRV and f_m is the largest for the weak IN fields. As we pointed out earlier, differences between correlations of ΔRV with f_m and $\langle fB \rangle_m$ could be influenced by the relations between field strengths and fluxes shown (Figure 5) and discussed in Section 4.1.1—the relative changes in average field strengths (flux densities) for a given amount of change in fill factor are much smaller for plages and spots than for network fields. Correlations between ΔRV and the total magnetic fill factor $f (= \sum_m f_m)$, full-disk-averaged unsigned magnetic flux $\langle |B| \rangle$, UV intensities at 1600 and 1700 Å (see Section 4.3), and $\log(R'_{HK})$ are shown in Figure 8. Although the correlation coefficients (marked within the panels in Figure 8) between the Sun-as-a-star spectroscopic quantities (ΔRV and $\log(R'_{HK})$ from HARPS-N) and the disk averages of resolved observations from SDO (HMI and AIA) all are very similar, we do note that the fill factors correlate stronger than the unsigned average magnetic flux. Among the chromospheric quantities, we find the disk-averaged UV intensities at 1700 Å correlate the strongest with the ΔRV s—we discuss these chromospheric activity proxies in detail in the following section.

4.3. UV Intensities at 1600 and 1700 Å as Magnetic Flux Proxies

The chromospheric Ca II K emission index $\log(R'_{HK})$ (Noyes et al. 1984) is a well-known observational quantity that acts as a proxy for the photospheric magnetic flux threading the chromospheric layers. It traces very well the strong supergranular network (NE) and the plage fields and hence correlates very well with the RV fluctuations (see Figure 6). It is also well known that UV emissions over wavelength bands centered at 1600 and 1700 Å originating in upper photospheric and chromospheric layers faithfully capture the underlying magnetic flux (Krijger et al. 2001). Here, we experiment with the same UV emission intensities imaged by SDO/AIA, extracted and processed as explained in Section 3. The disk-averaged intensities, $\langle I_{1600} \rangle$ and $\langle I_{1700} \rangle$, are derived from 1 hr cadence images averaged over a day (24 images) as for other HMI observables that we employed. The scatter plot of $\langle I_{1600} \rangle$ and

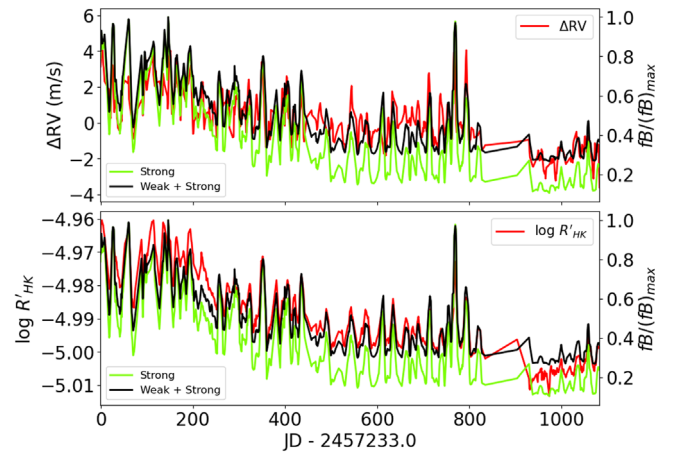


Figure 6. Comparison of variations in HARPS-N ΔRV (upper panel) and in $\log(R'_{HK})$ (lower panel), in red, with those in average unsigned magnetic fluxes of the strong field ($\langle fB \rangle_{spot} + \langle fB \rangle_{plage} + \langle fB \rangle_{NE}$) (in green), and that including the weak IN field (in black) covering 609 days over 2015–2018. Note that $\langle fB \rangle$ s are normalized with their maximum values to enable a comparison of the relative variations.

ΔRV is shown in panel (b) and that between $\langle I_{1700} \rangle$ and ΔRV in panel (c) of Figure 8; the correlation coefficients, respectively, are 0.75 and 0.77. While the former is the same as that between $\log(R'_{HK})$ and ΔRV , the $\langle I_{1700} \rangle$ correlates stronger with ΔRV . We also study the correlations of $\langle I_{1600} \rangle$, $\langle I_{1700} \rangle$ and $\log(R'_{HK})$ with the feature-specific f_m and $\langle fB \rangle_m$ of IN, NE, plage, and spot fields in Figures 9 and 10. Comparing the correlation coefficients in these plots, we find that UV intensities correlate significantly stronger with plages than the $\log(R'_{HK})$. A closer examination of panels for plage fields shows that the $\log(R'_{HK})$ tend to saturate at the largest fill factors (or high activity levels), while the UV intensities remain more linearly correlated. Noting that the data period used in this work (i.e., the period covered by HARPS-N solar observations) starts well past the Cycle 24 maximum, we expect that the slight saturation that we see in Ca II K emission would likely be much larger at cycle maximum activity levels. Hence, at high activity levels, the UV intensities would provide a better measure of plage fields and hence could be more reliable proxies for variations in RVs caused by these fields.

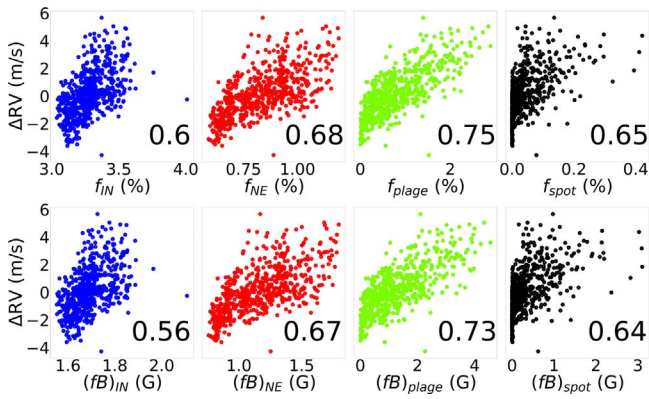


Figure 7. Correlations between ΔRV and the fill factors (f_m , upper panel), and average unsigned magnetic flux ($(fB)_m$, lower panel) of the different magnetic features, as indicated in axis labels. The Spearman correlation coefficients are given in each panel.

We note here that the saturation of chromospheric Ca II K emissions at high activity levels is well known and studied on the Sun (see, for example, Loukitcheva et al. 2009) as well as in a large number of other stars (e.g., Reiners et al. 2022).

4.4. Periodogram Analysis

Lomb–Scargle periodograms are commonly used to detect periodic signals due to planets in stellar RVs. While presenting the time series of f_m and $(fB)_m$, in Section 4.1, we have already discussed the typical timescales introduced by the evolution of magnetic flux in the different features, especially due to the decay of active region flux into weak IN fields and longer timescales involved in the reorganization of flux into NE fields. Here we examine their signatures that appear as power peaks in generalized Lomb–Scargle (GLS) periodograms (Zechmeister & Kürster 2009) and compare them with those of ΔRV . The results are shown in Figures 11–13. We mainly focus on shorter periodicities, especially the rotation period and shorter ones. Note also that the total time length of HARPS-N RVs is less than 3 yr. Comparisons of the GLS periodogram of ΔRV with that of feature-specific f_m s and $(fB)_m$ s are shown in Figures 11 and 12, respectively. The dominant periodicities seen are of rotation (27–30 days) and its first harmonic (13–15 days) in all the quantities, above the false alarm probability (FAP) of 0.001%. We note, in particular, the very similar periodicities present in the spectra of ΔRV and the weak IN fields over the short period range of between 7 and 10 days; although the FAP is between 10% and 1% for most of these short periods, we note a peak significantly above 1% FAP at 8–9 days for the IN fields in Figures 11 and 12. Although power peaks at the 9–10 day period, it corresponds to the third harmonic of the primary rotation period (27–30 days), and we note that the stronger NE and plage fields do not exhibit any significant peak at periods shorter than 10 days except perhaps the spot fields that have a dense set of peaks over a wide range of periods. Hence, we speculate that the origin of higher harmonics, especially the third harmonic period of 8–9 days in IN fields, is related to their latitudinal distribution and time evolution, which cause perhaps some beating interference with the rotation of the sunspot belt. Such a possible physical origin of periods close to the third harmonic is strengthened further below when we compare the periodograms of photospheric and chromospheric quantities. Given that we capture only about

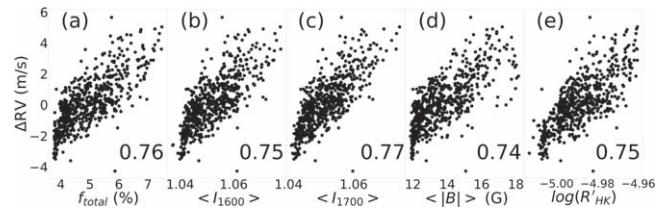


Figure 8. Correlations of HARPS-N ΔRV s with the five main parameters characterizing solar magnetic contributions: total fill factor, disk-averaged UV intensities at 1600 and 1700 Å, average unsigned magnetic field, and chromospheric Ca II K flux index (left to right). Spearman correlation coefficients are given in each panel.

one-third of the IN flux that is present on the Sun from SDO/HMI observations, we speculate that much of the shorter periods present in ΔRV are likely due to the weak IN fields. The sunspot fill factors and magnetic fluxes show a prominent cluster of peaks around 20 days, which are missing in the spectra of all the other quantities. Such peaks have been noted by several authors, and their origin has not been identified and analyzed so far. We do not further explore the origin of various harmonics of rotation period in the periodograms except by using the differences that are clearly associated with different magnetic features.

A comparison of GLS periodograms of spectroscopically derived Sun-as-a-star quantities, ΔRV , $\log(R'_{HK})$, and SORCE TSI and those of disk averages of resolved observations in UV intensities, $\langle I_{1600} \rangle$ and $\langle I_{1700} \rangle$, from SDO/AIA is shown in Figure 13. Interestingly, it is noted that the magnetic activity in the chromosphere as captured by $\log(R'_{HK})$ (panel (d)) and $\langle I_{1600} \rangle$ (panel (c)) do not exhibit any significant periods shorter than 10 days, while the other quantities of photospheric origin ΔRV (panel (e)), TSI (panel (a)) or that with significant photospheric contribution, $\langle I_{1700} \rangle$, do. Now among the different magnetic features, we see only the IN fields exhibit significant power at periods shorter than 10 days (Figures 11 and 12). This we speculate as being an indication that the weak IN fields are the cause of such short periodicities in ΔRV and TSI, as it is known that the footpoints of small-scale loops comprising IN fields do cause brightening in certain visible spectral bands such as the *G* band while their looping magnetic field not really reaching the chromosphere and thus not causing any significant emissions there (see Bellot Rubio & Orozco Suárez 2019 and references therein).

5. Discussion and Conclusion

The proximity of the Sun provides us opportunities to study in detail the complex interactions between convection and magnetic fields. Solar observations show that the structuring of magnetic fields in terms of strengths and fluxes (sizes), which in turn determine their characteristic thermal and mechanical appearances, is the result of complex magnetoconvective processes (Solanki et al. 2006). Our understanding that such processes derive from basic physical effects in MHD, viz. magnetic forces modifying the fluid motion, indicate that such magnetic structuring is expected in the photospheres of all stars like the Sun. Hence, it is hardly surprising that the magnetic activity causes jitter in stellar RVs, and that it is mainly through the suppression of convective blueshifts by photospheric magnetic fields (Cegla et al. 2018; Cegla 2019). However, we point out that we still lack a full understanding of the complex interplay between convection and magnetic fields

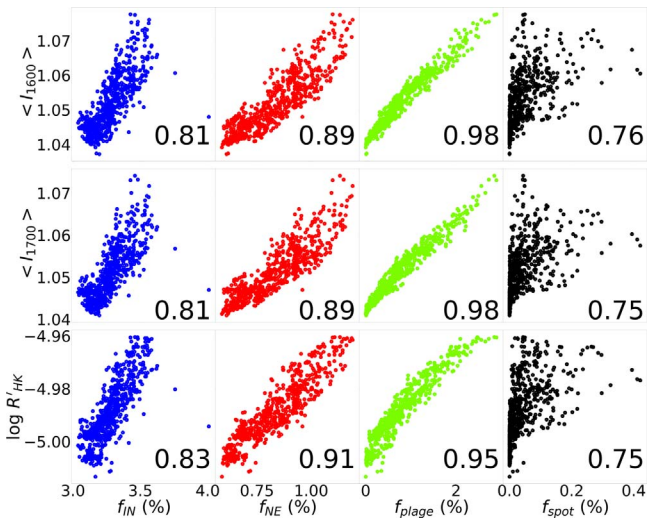


Figure 9. Correlations of fill factors of the different magnetic features with the average UV intensities at the wavelengths 1600 and 1700 Å, and the chromospheric Ca II K flux index (top to bottom). Spearman correlation coefficients are given in each panel.

even on the Sun, and hence lack a modeling capability to account for all the RV jitter that magnetic fields can cause (Crass et al. 2021; Newman et al. 2023).

In this paper, using disk-resolved images of magnetic fields and continuum intensities from SDO/HMI, we have attempted to incorporate physical connections between the evolution of different magnetic features on the solar surface to differentiate them better while studying their correlations with the RVs. Using hourly data from HMI (24 images per day), our analysis method resulted in identifying and separating the quiet-Sun weak IN magnetic fields, IN. Our results presented in Section 4.1 show that, despite its lower resolution of 1'', HMI observations do capture a significant amount of IN flux. For IN fields, high-resolution observations provide a mean longitudinal flux of about 9×10^{16} Mx (Bellot Rubio & Orozco Suárez 2019), which although is higher than HMI's detection limit of about 4.26×10^{16} Mx (corresponding to a σ of 8 G for HMI LOS measurements) our adopted 3σ cutoff means that we are only including IN fields with flux larger than about 10^{17} Mx. Hence, with the caveat that we miss a large amount of IN flux in our study here, we are still able to identify and measure the IN fields in HMI observations and distinguish them from the NE fields based on the above criteria drawn from the well-established physics behind the structuring of small-scale fields. Regarding the use of a flux limit to separate the IN and NE fields, although high-resolution observations broadly agree on such a value ($\sim 3 \times 10^{17}$ Mx) (Gošić et al. 2014; Prabhu et al. 2020), we note that it is not a strict limit as these fields have significantly broad distributions with observed peak fluxes dependent on the resolution of observations (Zhou et al. 2013) and hence it is always possible that there exist kilogauss NE elements with a slightly smaller flux and vice versa for IN elements because intermediate states of splitting and merging are a common occurrence in the dynamics of NE (Schrijver et al. 1997) and IN (Campbell et al. 2021) fields.

We note that the differing signatures of different magnetic features carry important information on the dynamical connections between the evolution of different magnetic flux

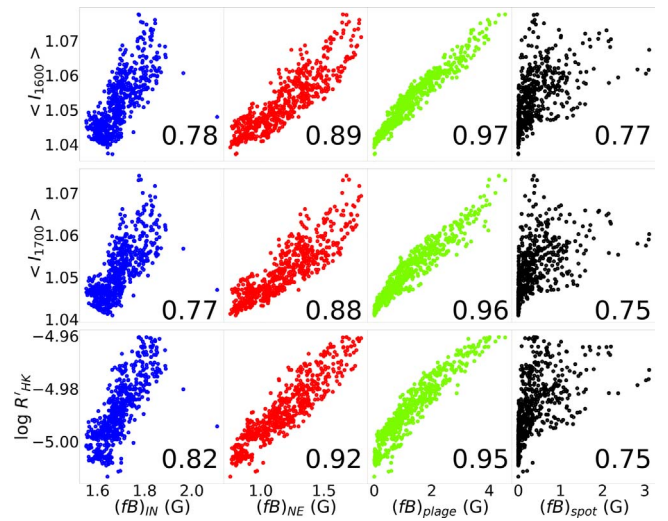


Figure 10. Correlations of the average unsigned magnetic flux of the different magnetic features with the average UV intensities at the wavelengths 1600 and 1700 Å, and the chromospheric flux index (top to bottom). Spearman correlation coefficients are given in each panel.

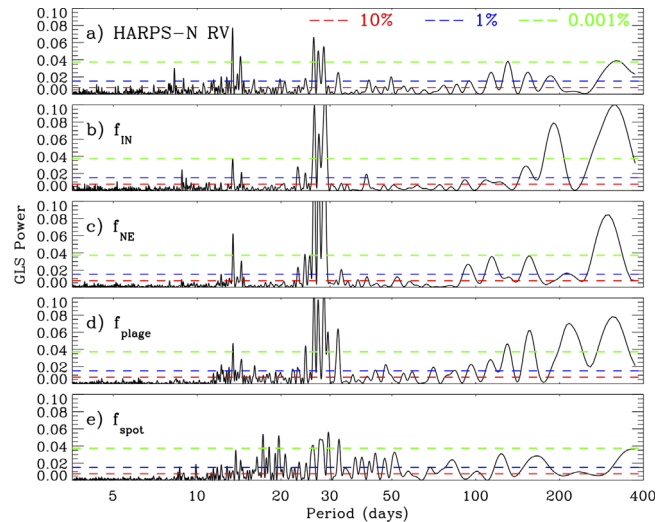


Figure 11. GLS periodograms of feature-specific fill factors f_m .

concentrations and their interactions with convective and other large-scale flows on the Sun. In the context of RV variations, we particularly note the characteristic short timescale fluctuations of IN fields, which at the same time change relatively very little over the longer cyclic timescale, compared to other features. This latter aspect of IN fields is also well appreciated in the solar literature (Bellot Rubio & Orozco Suárez 2019). We have shown that these two features of IN fields potentially introduce such timescales in the RV variations too (see Figures 6 and 12), while also confirming the previously reported dominant correlations between other magnetic structures (plages and spots) and RVs. And as shown in Sections 4.2 and 4.4, we are also able to distinguish the differing signatures of IN and NE fields in the HARPS-N RV variations (Figures 11 and 12). Such a contribution from IN fields is expected because the flux contained in them is significant (see Figure 3) and moreover they dominate the total flux during the solar minimum period as evident in the relative variations of $(fB)_m$ shown in Figure 4. The IN fields changing relatively little over

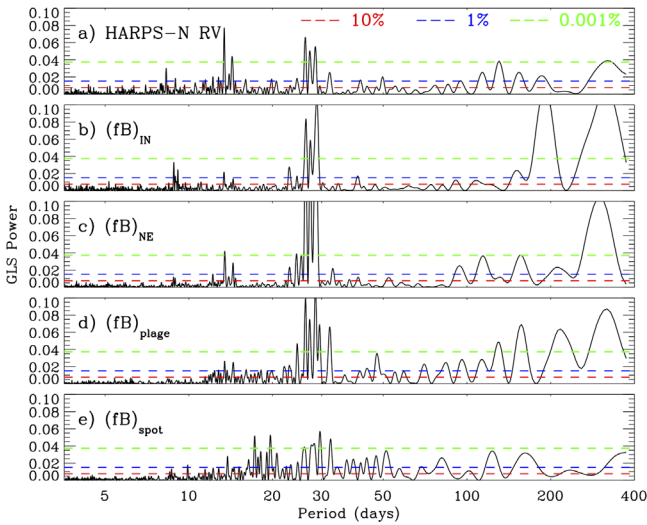


Figure 12. GLS periodograms of feature-specific average unsigned magnetic fluxes, $(fB)_m$.

the solar cycle perhaps cause a constant background signal in ΔRV . We stress that the relative constancy of IN on longer timescales, thus, is important to correctly determine the long-term baseline in the RV fluctuations due to magnetism: in the absence of full coverage of a solar minimum period, a mean-subtracted RV would be biased by the strongly varying contributions from active region fields and hence would cause an offset as can be seen in Figure 7. We further point out that weak background fluctuations from the IN fields on the long cycle timescale are of significant consequence for the following reasons: (i) we still do not understand the origin of the weak fields (holding a large fraction of the total flux) on the Sun (Lites et al. 2008; Bellot Rubio & Orozco Suárez 2019), although simulation studies show the possible operation of the so-called local (small-scale) dynamos with wider implications for stellar magnetism (Rempel et al. 2023; Warnecke et al. 2023), and (ii) such fields may be of greater relevance in other stars that possibly maintain them much more efficiently and hence extreme precision measurements of RVs of these stars should provide pathways to explore the existence of these fields and the underlying dynamo mechanisms. We note that at 1'' resolution SDO/HMI captures only about 1/3 of flux in IN (Khomenko & Collados 2006; Zhou et al. 2013), and hence our inferences on the contributions of IN to RV variations are likely to be much lower than the actual ones. We have also derived indications that correlations between fill factors and average unsigned magnetic fluxes of different magnetic features themselves may play a role in the differences between the correlations of area fill factors and average unsigned magnetic fluxes with RVs.

Further, we point out that the correlated variation between spots and IN fields, presented and discussed in Section 4.1 (see the insets in Figures 2 and 3), is related to the nature of decay of active region flux, wherein the larger content of spots decay directly to the weak IN on significantly shorter timescales than that of reorganization of such flux into more uniform super-granular NE fields. Hence, if NE indeed receives a major supply from decaying active regions then there will be a significant delay between the rise of spot flux and that in NE, depending on the timescales involved in the dispersal of all the decaying flux routed via the IN. Noting that, since the flux accumulating in it gets

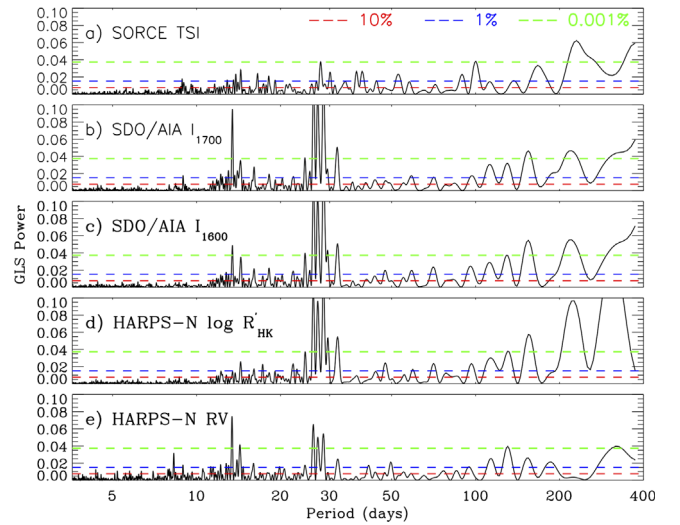


Figure 13. Comparison of GLS periodograms of photospheric TSI and ΔRV with those of chromospheric $\log(R'_{HK})$ and $\langle I_{1600} \rangle$.

intensified and brighter, the NE is a significant contributor to the TSI enhancements that compensate for reduction due to dark spots, the relationships between temporal variations of feature-specific f_m and $(fB)_m$ that we see in Figures 2 and 3 are likely behind those seen in the brightness variations contributed by faculae, network, and spots (Yeo et al. 2020).

With the aim of exploring and deriving additional diagnostics from UV emissions observed by SDO/AIA, we have experimented with disk-averaged emission intensities at wavelengths 1600 and 1700 Å, $\langle I_{1600} \rangle$ and $\langle I_{1700} \rangle$. These UV emissions are well known to capture the underlying magnetic flux in the photospheric and chromospheric heights, although the exact mechanisms of heating that cause emissions may differ depending on the height ranges and the spectral content of these two wavelength bands (Krijger et al. 2001). We have studied correlations of these UV emissions with different magnetic features, especially comparing them with those of spectroscopically derived Ca II K index $\log(R'_{HK})$ from HARPS-N. While we find that the disk-averaged UV intensities perform, in general, equally well as a chromospheric proxy for the magnetic flux behind the RV variations as $\log(R'_{HK})$, we also show that the UV intensities remain linearly correlated with plage magnetic flux at high activity levels, while the Ca II H-K emission indices tend to saturate. Within the time period of data used in this work, we observe only a slight saturation in $\log(R'_{HK})$ against plage fields (see Figures 9 and 10). However, at cycle maximum activity levels when the disk areas of the plage fields peak, the saturation of chromospheric Ca II K emissions is well known and studied on the Sun (see, for example, Loukitcheva et al. 2009). Such a phenomenon is also well observed in a large number of other Sun-like stars (see, for example, Reiners et al. 2022). Hence, our finding of stronger correlations between UV intensities ($\langle I_{1600} \rangle$ and $\langle I_{1700} \rangle$) and plage fields (Figures 9 and 10) point to a better utility of these emission measures in capturing contributions of plage fields to RVs, especially at high activity levels or in highly active stars, which saturate in chromospheric Ca II K emissions.

Lastly, through the analysis of the GLS periodogram (Zechmeister & Kürster 2009), we have identified short-term periodicities possibly arising from the dynamics of our newly characterized IN fields and have related them to such

periodicities seen in HARPS-N RV fluctuations (ΔRV). We have also noted that the power peaks at 9–10 day periods coincide with the third harmonic of the primary rotation period (27–30 days). However, since only the weak IN fields exhibit significant peaks at periods shorter than 10 days we have speculated that the higher (third) harmonics is possibly related to their spatial (latitudinal) distribution and time evolution, which interfere with that due to differential rotation. Another interesting feature that favors such an origin, related to the physical distribution of IN fields, of periods close to the third harmonic is the difference between periodograms of photospheric and chromospheric quantities: significant short-term periodicities (<10 days) appear only in the periodograms of photospheric observables, HARPS-N RV, SORCE TSI and slightly in $\langle I_{1700} \rangle$, but not in the chromospheric ones, $\log(R'_{HK})$ and $\langle I_{1600} \rangle$. Since only the IN fields, among the different magnetic features, exhibit periodicities shorter than 10 days (Figures 11 and 12), we conclude that the weak IN fields are the cause of such variations in ΔRV . This conclusion is strengthened further as the TSI is known to receive contributions from the footpoints of small-scale loops comprising IN fields, which do cause brightening in certain visible spectral bands such as the G band while their looping magnetic field does not reach the chromosphere and thus does not cause any significant emissions there (see Bellot Rubio & Orozco Suárez 2019 and references therein). Further, given that the origin of all the flux in IN and NE, which is more than 50% of the total flux on the Sun during activity maximum, is not yet fully understood (Lites et al. 2008; Bellot Rubio & Orozco Suárez 2019), dynamics of such magnetic fields in other stars, depending on their relative flux content with respect to other well-known features such as plages and spots, may play important roles in the variations of stellar RVs. A careful survey of precision RVs of Sun-like stars with varying activity levels will thus be important not only for exoplanet studies but also for understanding stellar magnetism.

Acknowledgments

The HMI and AIA data used are courtesy of the NASA/SDO and the HMI and AIA science teams. Data preparation

and processing have utilized the Data Record Management System (DRMS) software at the Joint Science Operations Center (JSOC) for NASA/SDO at Stanford University. HARPS-N solar data used are courtesy of the Geneva Observatory, the Center for Astrophysics in Cambridge (Massachusetts), the Universities of St. Andrews and Edinburgh, the Queen’s University Belfast, the UK Astronomy Technology Center, and the Italian Istituto Nazionale di Astrofisica. Data-intensive computations in this work have utilized the High-Performance Computing facility at the Indian Institute of Astrophysics. A.S. is supported by an INSPIRE Fellowship from the Department of Science and Technology (DST), Government of India. S.P.R. acknowledges support from the Science and Engineering Research Board (SERB, Government of India) grant CRG/2019/003786. We acknowledge communications with Dr. Xavier Dumusque on the latest version, ESPRESSO DRS 2.3.5, of the HARPS-N data pipeline for the RV and Ca II K data used in this work. We acknowledge the use of free packages of Python software. We thank our colleagues Harsh Mathur, T. Sivarani, Athira Unni, Swastik Chowbay, and Ravinder Banyal at the Indian Institute of Astrophysics for useful discussions. We thank an anonymous referee for a detailed review and suggestions, which resulted in substantive additions and improvements in the paper.

Author Contributions

S.P.R. contributed to the conception and design of the work reported in this paper. A.S. collected the data, developed the numerical codes, and carried out the computations. Both authors jointly worked on analyzing the calculations and interpreting the results. A first draft of the paper was written by A.S. S.P.R. worked on correcting and improving the presentation and prepared the final draft.

Appendix

Here, we present results from tests carried out comparing 45 and 720 s exposures HMI data, including different spatial binnings (2×2 and 4×4), to identify the cause of differences in fill factors of network magnetic fields, $f_{IN} + f_{NE}$, which is the sum of those of weak IN and strong NE fields (sum of the top

Table 1
Fill-factor Comparison with Those of Earlier Authors for Two Dates

Authors	Cadence	Spatial Binning	Spot(%)	Faculae(%) (Plage+IN+NE)	Plage(%)	IN+NE(%)	NE(%)	IN(%)
Date: 2011 November 10 at 00:01:30 UTC								
Haywood et al. (2016) (Figure 3)	45 s	No	0.4	9	NA	NA	NA	NA
This work	45 s	No	0.41	9.03	4.31	4.72	1.15	3.57
Date: 2015 November 28 at 20:00:00 UTC								
Milbourne et al. (2019)								
Haywood et al. (2022) (Figure 1)	720 s	Not known	0.03	3.25	1.59	1.66	NA	NA
Milbourne et al. (2021)								
This work	720 s	No	0.03	4.82	1.80	3.02	0.87	2.15
		2×2	0.03	4.30	1.71	2.59	0.96	1.63
		4×4	0.03	3.38	1.63	1.75	0.56	1.19
This work	45 s	No	0.03	5.98	1.81	4.17	0.94	3.23
		2×2	0.03	4.92	1.70	3.22	0.99	2.23
		4×4	0.03	3.43	1.58	1.85	0.57	1.28

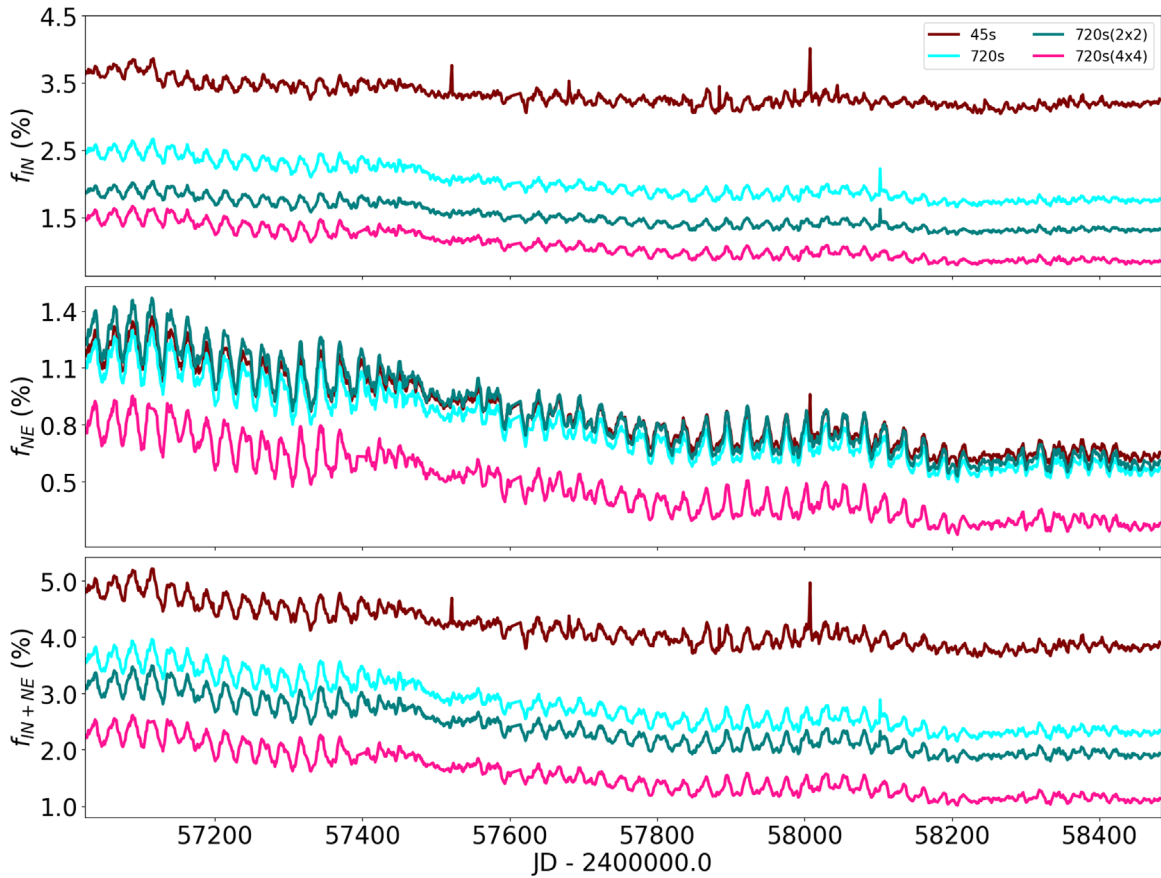


Figure 14. Comparison of fill factors f_{IN} , f_{NE} , and total network ($f_{ntwk} = f_{IN} + f_{NE}$) for 45 s cadence data (without binning), and 720 s cadence data sets (2×2 , 4×4 binning and without binning). See Section 4.1 for a discussion and summary of these results.

two panels of Figure 2), between our work and that of Milbourne et al. (2021) and Haywood et al. (2022; (f_{ntwk} in Figure 2 of Milbourne et al. 2021 or Figure 4 of Haywood et al. 2022). Figure 14 shows the results obtained from our repeat of analysis described in Section 3.1 using the 720 s exposure data from HMI with different levels of spatial binning.

These results for fill factors have to be compared with those presented in Figure 2 for 45 s data. Using the four sets of data, we find that the fill factors of large magnetized regions like spots and plage are not affected, as expected, whereas those of the small structures (IN, NE, and IN+NE) differ significantly for the different cadences and spatial binning used. We find that most of the previous studies have missed capturing a significant amount of these small-scale magnetic fields because of their use of 720 s cadence data set with a likely further 4×4 binning. A discussion and summary of these results are given in Section 4.1.

To compare specific numbers for fill factors with the previous studies, especially with those of Haywood et al. (2016) and Haywood et al. (2022), we tabulated results for the same dates (given in their papers) in Table 1. Haywood et al. (2016) use the original 45 s cadence LOS magnetogram data and explicitly mention the fill factors of sunspots and faculae (all non-spot fields), observed on 2011 November 10 at 00:01:30 UTC (in Figure 3 of Haywood et al. 2016). We find that our result matches exactly with that of Haywood et al. (2016). In a similar way, we have tested our result for the data set taken on 2015 November 28 at 20:00:00 UTC, to compare

with Figure 1 of Haywood et al. (2022). We find that our test results match the best with previous ones only after performing a 4×4 binning on the 720 s HMI LOS magnetogram.

ORCID iDs

Anisha Sen  <https://orcid.org/0000-0003-2694-3288>
S. P. Rajaguru  <https://orcid.org/0000-0003-0003-4561>

References

- Apai, D., Rackham, B. V., Giampapa, M. S., et al. 2018, arXiv:1803.08708
Barnes, W. T., Bobra, M. G., (The SunPy Community), et al. 2020, *ApJ*, **890**, 68
Bellot Rubio, L., & Orozco Suárez, D. 2019, *LRSP*, **16**, 1
Bertello, L., Ulrich, R. K., & Boyden, J. E. 2010, *SoPh*, **264**, 31
Boisse, I., Bouchy, F., Hébrard, G., et al. 2011, *A&A*, **528**, A4
Bose, S., & Nagaraju, K. 2018, *ApJ*, **862**, 35
Campbell, R. J., Mathioudakis, M., Collados, M., et al. 2021, *A&A*, **647**, A182
Cegla, H. 2019, *Geosc*, **9**, 114
Cegla, H. M., Watson, C. A., Shelyag, S., et al. 2018, *ApJ*, **866**, 55
Chatterjee, S., Banerjee, D., & Ravindra, B. 2016, *ApJ*, **827**, 87
Collier Cameron, A., Mortier, A., Phillips, D., et al. 2019, *MNRAS*, **487**, 1082
Crass, J., Gaudi, B. S., Leifer, S., et al. 2021, arXiv:2107.14291
Dravins, D., Lindegren, L., & Nordlund, A. 1981, *A&A*, **96**, 345
Dumusque, X., Boisse, I., & Santos, N. C. 2014, *ApJ*, **796**, 132
Dumusque, X., Cretignier, M., Sosnowska, D., et al. 2021, *A&A*, **648**, A103
Dumusque, X., Glenday, A., Phillips, D. F., et al. 2015, *ApJL*, **814**, L21
Fossum, A., & Carlsson, M. 2005, *Natur*, **435**, 919
Gošić, M., Bellot Rubio, L. R., Orozco Suárez, D., Katsukawa, Y., & del Toro Iniesta, J. C. 2014, *ApJ*, **797**, 49
Haywood, R. D., Collier Cameron, A., Unruh, Y., et al. 2016, *MNRAS*, **457**, 3637

- Haywood, R. D., Milbourne, T. W., Saar, S. H., et al. 2022, *ApJ*, 935, 6
- Hoeksema, J. T., Liu, Y., Hayashi, K., et al. 2014, *SoPh*, 289, 3483
- Khomenko, E., & Collados, M. 2006, in ASP Conf. Ser. 358, Solar Polarization 4, ed. R. Casini & B. W. Lites (San Francisco, CA: ASP), 42
- Kopp, G., & Lawrence, G. 2005, *SoPh*, 230, 91
- Kopp, G., Heuerman, K., & Lawrence, G. 2005, *SoPh*, 230, 111
- Krijger, J. M., Rutten, R. J., Lites, B. W., et al. 2001, *A&A*, 379, 1052
- Lefebvre, S., Ulrich, R., Webster, L., et al. 2005, *MmSAI*, 76, 862
- Lemen, J. R., Akin, D. J., Boerner, P. F., et al. 2011, *The Solar Dynamics Observatory* (Berlin: Springer), 17
- Lin, H. 1995, *ApJ*, 446, 421
- Lites, B. W. 2002, *ApJ*, 573, 431
- Lites, B. W., Kubo, M., Socas-Navarro, H., et al. 2008, *ApJ*, 672, 1237
- Lites, B. W., Leka, K. D., Skumanich, A., Martinez Pillet, V., & Shimizu, T. 1996, *ApJ*, 460, 1019
- Liu, Y., Hoeksema, J., Scherrer, P., et al. 2012, *SoPh*, 279, 295
- Loukitcheva, M., Solanki, S. K., & White, S. M. 2009, *A&A*, 497, 273
- Luhn, J. K., Ford, E. B., Guo, Z., et al. 2023, *AJ*, 165, 98
- Mayor, M., & Queloz, D. 1995, *Natur*, 378, 355
- Meunier, N., Lagrange, A. M., Mbemba Kabuiku, L., et al. 2017, *A&A*, 597, A52
- Milbourne, T., Haywood, R., Phillips, D., et al. 2019, *ApJ*, 874, 107
- Milbourne, T., Phillips, D., Langellier, N., et al. 2021, *ApJ*, 920, 21
- Newman, P. D., Plavchan, P., Burt, J. A., et al. 2023, *AJ*, 165, 151
- Noyes, R. W., Hartmann, L. W., Baliunas, S. L., Duncan, D. K., & Vaughan, A. H. 1984, *ApJ*, 279, 763
- Parker, E. 1978, *ApJ*, 221, 368
- Phillips, D. F., Glenday, A. G., Dumusque, X., et al. 2016, *Proc. SPIE*, 9912, 99126Z
- Prabhu, A., Lagg, A., Hirzberger, J., & Solanki, S. K. 2020, *A&A*, 644, A86
- Rajaguru, S. P., & Hasan, S. S. 2000, *ApJ*, 544, 522
- Reiners, A., Shulyak, D., Käpylä, P. J., et al. 2022, *A&A*, 662, A41
- Rempel, M., Bhatia, T., Bellot Rubio, L., & Korpi-Lagg, M. J. 2023, *SSRv*, 219, 36
- Scherrer, P. H., Schou, J., Bush, R., et al. 2012, *SoPh*, 275, 207
- Schou, J., Scherrer, P. H., Bush, R. I., et al. 2012, *SoPh*, 275, 229
- Schrijver, C. J., & Harvey, K. L. 1994, *SoPh*, 150, 1
- Schrijver, C. J., Title, A. M., van Ballegoijen, A. A., Hagenaar, H. J., & Shine, R. A. 1997, *ApJ*, 487, 424
- Solanki, S. K., Inhester, B., & Schüssler, M. 2006, *RPPH*, 69, 563
- Solanki, S. K., Zufferey, D., Lin, H., Ruedi, I., & Kuhn, J. R. 1996, *A&A*, 310, L33
- Spruit, H. 1979, *SoPh*, 61, 363
- Thompson, W. 2006, *A&A*, 449, 791
- Venkatakrishnan, P. 1986, *Natur*, 322, 156
- Wachter, R., Schou, J., Rabello-Soares, M., et al. 2011, *The Solar Dynamics Observatory* (Berlin: Springer), 261
- Warnecke, J., Korpi-Lagg, M. J., Gent, F. A., & Rheinhardt, M. 2023, *NatAs*, 7, 662
- Yeo, K., Solanki, S., & Krivova, N. 2013, *A&A*, 550, A95
- Yeo, K. L., Solanki, S. K., & Krivova, N. A. 2020, *A&A*, 639, A139
- Zechmeister, M., & Kürster, M. 2009, *A&A*, 496, 577
- Zhou, G., Wang, J., & Jin, C. 2013, *SoPh*, 283, 273